photonics

MDPI

Article

Simultaneous Compensation for Perturbed Dual-Channel Telescopes Based on Nodal Aberration Theory

Mengmeng Xu [1,2,3], Qihao Wang [1,2,3], Yuan Yao [1,4], Weijie Deng [1,2,3], Donglin Xue [1,2,3,*] and Xuejun Zhang [1,2,3]

[1] Changchun Institute of Optics, Fine Mechanics and Physics, Chinese Academy of Sciences, Changchun 130033, China
[2] University of Chinese Academy of Sciences, Beijing 100049, China
[3] State Key Laboratory of Advanced Manufacturing for Optical Systems, Changchun 130033, China
[4] State Key Laboratory of Dynamic Optical Imaging and Measurement, Changchun 130033, China
* Correspondence: xuedl@ciomp.ac.cn

Abstract

Active compensation for perturbed space telescopes is an effective means of improving the image quality. In common-aperture dual-channel telescopes, compensation can only be achieved by adjusting a shared secondary mirror (SM), making it difficult to balance the inconsistent misalignment aberrations between the channels. To address this issue, an analytic method for simultaneous compensation of dual-channel aberrations is proposed. Based on the improved Nodal Aberration Theory (NAT), the analytic solution for the common compensation position of the SM is derived by establishing a geometric balance between the aberration field nodes in the image planes of the two channels. On this basis, the theoretical conditions required for the consistency of the optimal compensation positions in the dual channels are also presented. The robustness of the method is validated through Monte Carlo simulations under conditions of random noise and surface figure errors. The results show that the average RMS wavefront error (WFE) of each channel is reduced to less than $\lambda/16$ (λ = 632.8 nm) after compensation under various misalignment conditions. Compared with the traditional Sensitivity Matrix Method (SMM), the proposed method exhibits superior compensation accuracy and decoupling capability in correcting dual-channel aberrations, thereby significantly improving the optical performance of the system.

Keywords: common-aperture; nodal aberration theory; dual-channel telescopes; simultaneous compensation

1. Introduction

With the growing demand for high-resolution Earth observation and astronomical exploration, space optical payloads are developing toward larger apertures and multi-functionality. Compared with traditional single-channel space telescopes, common-aperture multi-channel systems can simultaneously achieve multiple imaging functions by sharing the primary optical system, significantly improving observation efficiency. This compact architecture reduces the optical component count and spatial envelope, meeting the lightweight and miniaturization requirements of space payloads.

As the apertures of space telescopes continue to increase, mirrors are susceptible to environmental perturbations such as vibration, gravity release, and thermal gradients. These perturbations induce both figure errors and misalignments of each mirror that significantly degrade image quality. To solve this problem, active optical compensation

Received: 21 January 2026
Revised: 3 February 2026
Accepted: 6 February 2026
Published: 14 February 2026

by adjusting the secondary mirror (SM) is a widely adopted strategy [1–5]. In common-aperture dual-channel optical systems, the two channels share the primary mirror (PM) and SM, and the aberrations in both channels must be compensated simultaneously by adjusting the shared SM. However, since the two channels often possess distinct optical parameters such as focal length and field of view, their sensitivities to SM misalignment differ. Consequently, adjusting the SM to optimize one channel may inadvertently degrade the performance of the other. Correcting aberrations in such systems is not merely a matter of structural coupling but requires resolving the conflicting optical compensation requirements between the channels, which is significantly more complex than in single-channel systems.

Active optical compensation strategies for space telescopes are mainly classified into two categories: numerical optimization and analytical methods. The numerical method represented by the Sensitivity Matrix Method (SMM) is widely used in engineering practice because of its easy implementation [6]. This method usually utilizes numerical differentiation to construct a linear mapping table that relates the wavefront Zernike coefficients to the degrees of freedom (DOFs) of the SM [7,8], and the solution accuracy is affected by nonlinearity. In some systems, the sensitivity matrix is ill-conditioned or singular due to parameter coupling, leading to numerical iterative methods unstable or slow to converge. Especially in multi-channel optical systems, it is difficult to achieve a globally optimal balance for the system. In contrast, Nodal Aberration Theory (NAT) provides an analytic method [9,10], and reveals that misalignments lead to predictable vector shifts at the nodes of the aberration field [11,12]. NAT offers a theoretical basis for decoupling the misalignment states, making it particularly suitable for complex optical systems. Recent studies by Jiang, Wang, and Sebag et al. have successfully applied NAT to the alignment of three-mirror anastigmatic (TMA) telescopes [13,14]. Additionally, Zhang and Bai proposed optical compensation strategies for the perturbed TMA telescopes [15–17]. However, these methods based on NAT were focused on single-channel systems, and some new work should be done for common-aperture dual-channel systems.

In this paper, an analytic method for the common compensation of dual-channel misalignment by the SM is proposed based on NAT, ensuring high image quality for both channels. We derive the theoretical conditions required for the consistency of the dual-channel optimal compensation positions. The effectiveness of the proposed method is validated through simulations considering random noise and surface figure errors. Furthermore, a comparative analysis demonstrates that our method outperforms the traditional SMM in terms of solution accuracy and robustness.

2. Theory and Method

2.1. Compensation Algorithm Based on Improved Third-Order NAT

The vector form of the wave aberration for a perturbed optical system can be expressed as [18,19]

$$W = \sum_j \sum_p^{\infty} \sum_n^{\infty} \sum_m^{\infty} W_{klm,j} \left[\left(\vec{H} - \vec{\sigma}_j \right) \cdot \left(\vec{H} - \vec{\sigma}_j \right) \right]^p \left(\vec{\rho} \cdot \vec{\rho} \right)^n \left[\left(\vec{H} - \vec{\sigma}_j \right) \cdot \vec{\rho} \right]^m \quad (1)$$

where $\vec{\sigma}_j$ is the aberration field displacement vector for surface j, $W_{klm,j}$ is the corresponding wave aberration coefficient, $\vec{H}$ is the normalized field vector, $\vec{\rho}$ is the normalized pupil vector.

In a perturbed optical system, coma and astigmatism are the dominant aberrations. Based on third-order and fifth-order aberrations [20,21], the contributions of coma and astigmatism for the perturbed optical system are given by

$$\begin{aligned} W_{COMA} &= \left[\left(W_{131}\vec{H}-\vec{A}_{131}\right)\cdot\vec{\rho}\right]\left(\vec{\rho}\cdot\vec{\rho}\right)+\left[\left(W_{151}\vec{H}-\vec{A}_{151}\right)\cdot\vec{\rho}\right]\left(\vec{\rho}\cdot\vec{\rho}\right)^2+ \\ &\left[\begin{pmatrix} W_{331M}\left(\vec{H}\cdot\vec{H}\right)\vec{H}-2\left(\vec{H}\cdot\vec{A}_{331M}\right)\vec{H}+2B_{331M}\vec{H}- \\ \left(\vec{H}\cdot\vec{H}\right)\vec{A}_{331M}+B_{331M}^2\vec{H}^*-C_{331M} \end{pmatrix}\cdot\vec{\rho}\right]\left(\vec{\rho}\cdot\vec{\rho}\right) \end{aligned} \tag{2}$$

$$\begin{aligned} W_{AST} &= \tfrac{1}{2}\left[W_{222}\vec{H}^{2}-2\vec{H}A_{222}+\vec{B}_{222}^{2}\right]\cdot\vec{\rho}^{2}+\tfrac{1}{2}\left[\left(W_{242}\vec{H}^{2}-2\vec{H}A_{242}+\vec{B}_{242}^{2}\right)\cdot\vec{\rho}^{2}\right]\left(\vec{\rho}\cdot\vec{\rho}\right) \\ &+\tfrac{1}{2}\left[\begin{array}{l} W_{422}\left(\vec{H}\cdot\vec{H}\right)\vec{H}^{2}-2\left(\vec{H}\cdot\vec{H}\right)\left(\vec{H}A_{222}\right)+3\left(\vec{H}\cdot\vec{H}\right)\vec{B}_{422}^{2}- \\ 2\left(\vec{H}\cdot A_{222}\right)\vec{H}^{2}+3B_{422}\vec{H}^{2}-3\vec{H}C_{422}-C_{422}^{3}\vec{H}^{*}+\vec{D}_{422}^{2} \end{array}\right]\cdot\vec{\rho}^{2} \end{aligned} \tag{3}$$

where $W_{klm}=\sum_j W_{klmj}$, $\vec{A}_{klm}=\sum_j W_{klmj}\vec{\sigma}_j$, $\vec{B}_{klm}^{2}=\sum_j W_{klmj}\vec{\sigma}_j^{2}$, $\vec{B}_{klm}=\sum_j W_{klmj}\left(\vec{\sigma}_j\cdot\vec{\sigma}_j\right)$, $\vec{C}_{klm}^{3}=\sum_j W_{klmj}\vec{\sigma}_j^{3}$, $\vec{D}_{klm}^{2}=\sum_j W_{klmj}\left(\vec{\sigma}_j\cdot\vec{\sigma}_j\right)\vec{\sigma}_j^{2}$, $\vec{H}^*$ represents the complex conjugate of the field vector $\vec{H}$.

In optical testing, the wavefront at the exit pupil is usually fitted to Zernike polynomials to represent the measured wavefront. In the form of Zernike polynomials [22], the wave aberration for the perturbed system is expressed as

$$W=\sum_i\left[\sum_k^{\infty}\sum_l^{\infty}\sum_m^{\infty}\sum_a^{\infty}\vec{f}_{klm}^{\,a}\left(H_x,H_y\right)\cdot\vec{A}_{klm}^{\,a}\left(\vec{\sigma}_x,\vec{\sigma}_y\right)\right]_i Z_i(\rho,\varphi)=\sum_i C_i\left(H_x,H_y\right)Z_i(\rho,\varphi) \tag{4}$$

where $Z_i(\rho,\varphi)$ is the Zernike term, $C_i\left(H_x,H_y\right)$ is the corresponding Zernike coefficient, $\vec{H}_x$ and $\vec{H}_y$ represent the x-component and y-component of $\vec{H}$, while $\vec{\sigma}_x$, $\vec{\sigma}_y$ represent the x-component and y-component of $\vec{\sigma}$. ρ and φ represent the components of $\vec{\rho}$, and a represents the power of the aberration field displacement vector $\vec{\sigma}$. $\vec{A}_{klm}^{\,a}\left(\vec{\sigma}_x,\vec{\sigma}_y\right)$ is an unnormalized displacement vector in the image plane. $\vec{f}_{klm}^{\,a}\left(H_x,H_y\right)$ is a vector describing the corresponding dependence of field-of-view (FOV). Equation (4) can be further expanded as

$$\sum_k^{\infty}\sum_l^{\infty}\sum_m^{\infty}\left[\begin{array}{l}\vec{f}_{klm}^{\,0}\left(H_x,H_y\right)\cdot\vec{A}_{klm}^{\,0}\left(\vec{\sigma}_x,\vec{\sigma}_y\right)+\vec{f}_{klm}^{\,1}\left(H_x,H_y\right)\cdot\vec{A}_{klm}^{\,1}\left(\vec{\sigma}_x,\vec{\sigma}_y\right) \\ +\sum_{a=2}^{\infty}\vec{f}_{klm}^{\,a}\left(H_x,H_y\right)\cdot\vec{A}_{klm}^{\,a}\left(\vec{\sigma}_x,\vec{\sigma}_y\right)\end{array}\right]=C\left(H_x,H_y\right) \tag{5}$$

with

$$\sum_k^{\infty}\sum_l^{\infty}\sum_m^{\infty}\vec{f}_{klm}^{\,0}\left(H_x,H_y\right)\cdot\vec{A}_{klm}^{\,0}\left(\vec{\sigma}_x,\vec{\sigma}_y\right)=C_{nominal}\left(H_x,H_y\right) \tag{6}$$

where $C_{nominal}$ represents the intrinsic residual error of the nominal optical system.

As the aperture of the optical system increases, environmental factors such as vibration, air turbulence, and temperature gradient variations can affect the accuracy of wavefront measurements, resulting in lower fitting accuracy for high-order Zernike coefficients. In this paper, only the first 9 terms of the Fringe Zernike coefficients are considered. For the perturbed system, the SM is used to compensate for the misalignment aberrations. The

aberrations introduced by the adjustment of the SM are mainly third-order aberrations. Combining this with Equation (6), then

$$\frac{1}{3}\begin{bmatrix}-1 & 0\\ 0 & -1\end{bmatrix}\begin{bmatrix}\vec{A}_{131,x}\\ \vec{A}_{131,y}\end{bmatrix}=\begin{bmatrix}\Delta C_7\\ \Delta C_8\end{bmatrix} \tag{7}$$

$$\frac{1}{2}\begin{bmatrix}-H_x & H_y & 1 & 0\\ -H_y & -H_x & 0 & 1\end{bmatrix}\begin{bmatrix}2\vec{A}_{222,x}\\ 2\vec{A}_{222,y}\\ \vec{B}^{2}_{222,x}\\ \vec{B}^{2}_{222,y}\end{bmatrix}=\begin{bmatrix}\Delta C_5\\ \Delta C_6\end{bmatrix} \tag{8}$$

where $\Delta C_5 = C_5 - C_{5,nominal}$, $\Delta C_6 = C_6 - C_{6,nominal}$, $\Delta C_7 = C_7 - C_{7,nominal}$, $\Delta C_8 = C_8 - C_{8,nominal}$, C_5 and C_6 denote the 5th and 6th Fringe Zernike coefficients, C_7 and C_8 denote the 7th and 8th Fringe Zernike coefficients, $\vec{A}_{131,x}$ and $\vec{A}_{131,y}$ are the x-component and the y-component of $\vec{A}_{131}$.

The displacement vectors $\vec{A}_{klm}$ in the image plane are expressed as

$$\vec{A}_{131} = -\vec{A}_{131,SM} = -W^{sph}_{131,SM}\vec{\sigma}^{sph}_{SM} - W^{asph}_{131,SM}\vec{\sigma}^{asph}_{SM} \tag{9}$$

$$\vec{A}_{222} = -\vec{A}_{222,SM} = -W^{sph}_{222,SM}\vec{\sigma}^{sph}_{SM} - W^{asph}_{222,SM}\vec{\sigma}^{asph}_{SM} \tag{10}$$

By solving Equations (9) and (10), the aberration field displacement vectors of the SM ($\vec{\sigma}^{sph}_{SM}$, $\vec{\sigma}^{asph}_{SM}$) can be determined. According to the method based on paraxial ray trace equations [23], the compensation parameters for the SM can be determined using the following equations:

$$\vec{\sigma}^{sph}_{SM,x} = -\frac{BDE_{SM} + c_{SM}XDE_{SM}}{\vec{u}_{PM}(1 + c_{SM}d_1)} \tag{11}$$

$$\vec{\sigma}^{sph}_{SM,y} = \frac{ADE_{SM} - c_{SM}YDE_{SM}}{\vec{u}_{PM}(1 + c_{SM}d_1)} \tag{12}$$

$$\vec{\sigma}^{asph}_{SM,x} = -\frac{XDE_{SM}}{\vec{u}_{PM}d_1} \tag{13}$$

$$\vec{\sigma}^{asph}_{SM,y} = -\frac{YDE_{SM}}{\vec{u}_{PM}d_1} \tag{14}$$

where $\vec{u}_{PM}$ is the incident angle of the marginal chief ray on the PM, d_1 is the distance from the primary mirror to the SM, c_{SM} is the curvature of the SM, d_2 is the distance from the SM to the TM, c_{TM} is the curvature of the tertiary mirror (TM). These parameters are constants.

2.2. Analytic Solution for the Simultaneous Compensation Position of the SM

In a common-aperture dual-channel telescope, when the misalignment aberrations of the two channels are inconsistent, compensating one channel to its optimal state can lead to significant degradation in the image quality of the other channel. Therefore, the SM is required to correct the misalignment aberrations of both channels simultaneously.

For the perturbed optical system, the position of the node in the normalized image field shifts to the point indicated by the vector $\vec{a}_{klm}$, which can be expressed as

$$\vec{a}_{klm} = \frac{\vec{A}_{klm}}{W_{klm}} = \frac{\sum_j W_{klmj}\vec{\sigma}_j}{W_{klm}} \tag{15}$$

The node positions of the aberration fields are obtained in the normalized image plane as shown in Figure 1.

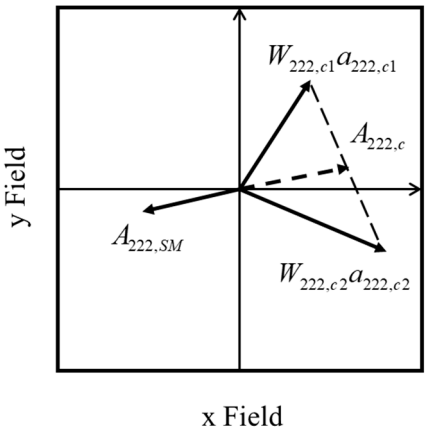

Figure 1. Node positions in the image plane.

Based on the displacement vectors $W_{klm,c1}\vec{a}_{klm,c1}$ and $W_{klm,c2}\vec{a}_{klm,c2}$ of the two channels, the center position is calculated as

$$\vec{A}_{klm,c} = \frac{1}{2}\left(W_{klm,c1}\vec{a}_{klm,c1} + W_{klm,c2}\vec{a}_{klm,c2}\right) \tag{16}$$

To balance the image quality of the two channels, the un-normalized displacement vector in the image plane corresponding to the compensation position is given by

$$\vec{A}_{klm,SM} = -\vec{A}_{klm,c} \tag{17}$$

The displacement vector of the SM is expressed as

$$-2\begin{bmatrix} W^{sph}_{222,SM} & W^{asph}_{222,SM} & 0 & 0 \\ 0 & 0 & W^{sph}_{222,SM} & W^{asph}_{222,SM} \\ W^{sph}_{131,SM} & W^{asph}_{131,SM} & 0 & 0 \\ 0 & 0 & W^{sph}_{131,SM} & W^{asph}_{131,SM} \end{bmatrix} \cdot \begin{bmatrix} \vec{\sigma}^{sph}_{SM,x} \\ \vec{\sigma}^{asph}_{SM,x} \\ \vec{\sigma}^{sph}_{SM,y} \\ \vec{\sigma}^{asph}_{SM,y} \end{bmatrix} = \begin{bmatrix} W_{222,c1}\vec{a}_{222,c1,x} + W_{222,c2}\vec{a}_{222,c2,x} \\ W_{222,c1}\vec{a}_{222,c1,y} + W_{222,c2}\vec{a}_{222,c2,y} \\ W_{131,c1}\vec{a}_{222,c1,x} + W_{131,c2}\vec{a}_{222,c2,x} \\ W_{131,c1}\vec{a}_{222,c1,y} + W_{131,c2}\vec{a}_{222,c2,y} \end{bmatrix} \tag{18}$$

Consequently, the simultaneous compensation parameters for the SM can be determined using Equations (11)–(14).

2.3. Theoretical Conditions for Consistent Optimal Compensation Positions

To ensure optimal performance, third-order coma and third-order astigmatism must be fully corrected for each channel. When the optimal compensation positions of the SM for the two channels are consistent, the displacement vectors of the third-order coma and third-order astigmatism in the image plane must also be consistent. This is expressed as

$$\vec{A}_{131,c1} = \vec{A}_{131,c2} \tag{19}$$

$$\vec{A}_{222,c1} = \vec{A}_{222,c2} \tag{20}$$

Since the aberration field displacement vector is typically a small quantity (generally $\vec{B}_{222}^{2} \approx 0$), based on Equations (7) and (8), the theoretical conditions for the consistency of the optimal compensation positions for the two channels are derived as

$$\Delta C_{7,c1} = \Delta C_{7,c2} \tag{21}$$

$$\Delta C_{8,c1} = \Delta C_{8,c2} \tag{22}$$

$$\frac{(\Delta C_{5,c1})^2 + (\Delta C_{6,c1})^2}{H_{x,c1}^2 + H_{y,c1}^2} = \frac{(\Delta C_{5,c2})^2 + (\Delta C_{6,c2})^2}{H_{x,c2}^2 + H_{y,c2}^2} \tag{23}$$

where $C_{i,c1}$ denote the Fringe Zernike coefficients for channel 1, and $C_{i,c2}$ denote the Fringe Zernike coefficients for channel 2.

Equations (21)–(23) reveal that compensation by decentration and tilt of the SM primarily induces field-constant coma and linear astigmatism.

3. A Common-Aperture Dual-Channel Four-Mirror Optical System

In this section, we present the design of a common-aperture dual-channel telescope with shared PM and SM. The optical layout of the system is shown in Figure 2. The system includes a visible light area-array channel and a visible light linear-array channel. The entrance pupil diameter of the optical system is 1800 mm. The focal length of the area-array channel is 25,200 mm with a $0.3^\circ \times 0.3^\circ$ field of view (FOV) and a 0.28° field offset. The focal length of the linear-array channel is 21,600 mm with a $1^\circ \times 0.1^\circ$ FOV and a -0.22° field offset. Each channel is composed of four mirrors: three aspheric mirrors and a spherical fourth mirror (FM). The aperture stop is located on the PM.

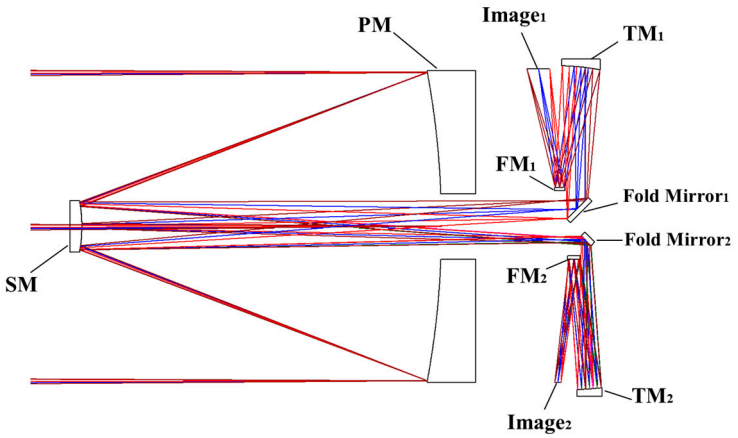

Figure 2. Optical design of the common-aperture dual-channel telescope.

The optical parameters are listed in Tables 1 and 2. The wave aberration coefficients are listed in Table 3.

Table 1. Optical parameters of the telescope in Channel 1.

Surface	Radius (mm)	Thickness (mm)	Conic Constant
PM (stop)	−4886.25	−2100	−0.9931
SM	−781.850	2788.6	−1.5653
Fold Mirror$_1$	Infinity	−936.6	-
TM$_1$	1207.931	710.1	−0.9764
FM$_1$	−4039.971	692.041	0
Image	Infinity	-	-

Table 2. Optical parameters of the telescope in Channel 2.

Surface	Radius (mm)	Thickness (mm)	Conic Constant
PM (stop)	−4886.25	−2100	−0.9931
SM	−781.850	2862.2	−1.5653
Fold Mirror$_2$	Infinity	−952.9	-
TM$_2$	1394.414	763.1	−1.2987
FM$_2$	−2792.498	−721.85	0
Image	Infinity	-	-

Table 3. Wave aberration coefficients of the dual-channel optical system.

Surface	W_{131}^{sph}	W_{131}^{asph}	W_{222}^{sph}	W_{222}^{asph}
SM	244.0339	217.7073	−43.1579	35.872

The design performance of the dual-channel telescope over the full field of view is illustrated in Figures 3 and 4. Fringe Zernike astigmatism (C5/6), Fringe Zernike coma (C7/8), and RMS wavefront error (WFE) are presented using Full-Field Displays (FFDs). The red spots in Figures 3c and 4c represent nine typical FOV points selected for calculating misalignments. As observed in Figures 3 and 4, the low residual aberration of the system is achieved through the balancing of third-order, fifth-order, and higher-order aberrations.

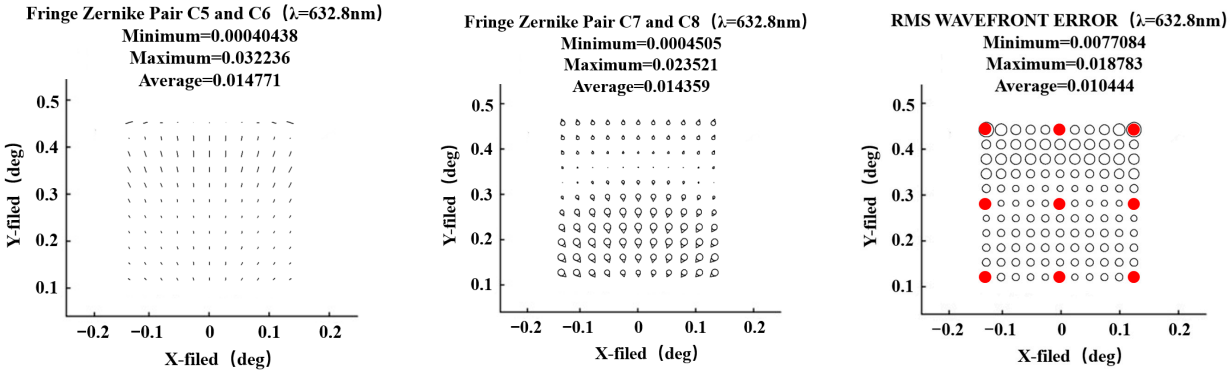

Figure 3. FFDs of the nominal optical system in Channel 1. (**a**) Fringe Zernike astigmatism (C5/6), (**b**) Fringe Zernike coma (C7/C8), (**c**) RMS WFE.

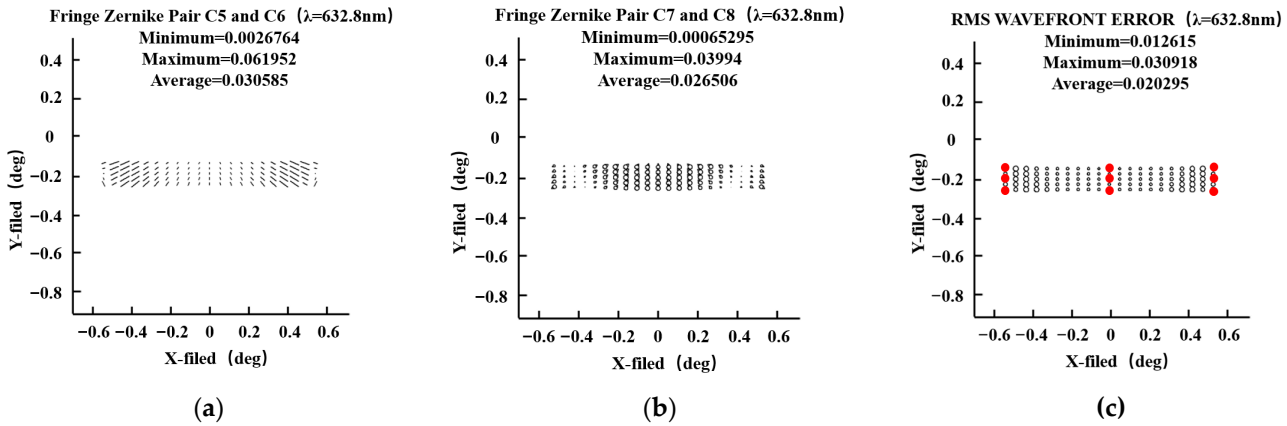

Figure 4. FFDs of the nominal optical system in Channel 2. (**a**) Fringe Zernike astigmatism (C5/6), (**b**) Fringe Zernike coma (C7/C8), (**c**) RMS WFE.

4. Simulation and Analysis

4.1. Simulation Results of the Common Compensation Method

In this section, the misalignment parameters of the SM and TM used in the simulation are listed in Table 4.

Table 4. Misalignments of the SM and TM.

	XDE (mm)	YDE (mm)	ADE (°)	BDE (°)
SM	0.05	−0.06	0.005	−0.008
TM_1	−0.06	0.10	0.006	0.010
TM_2	−0.10	−0.05	−0.008	0.005

In the simulation, nine measured field points were used, and four alignment iterations were performed on the misaligned system. The variations in the RMS WFE for both channels are shown in Figure 5.

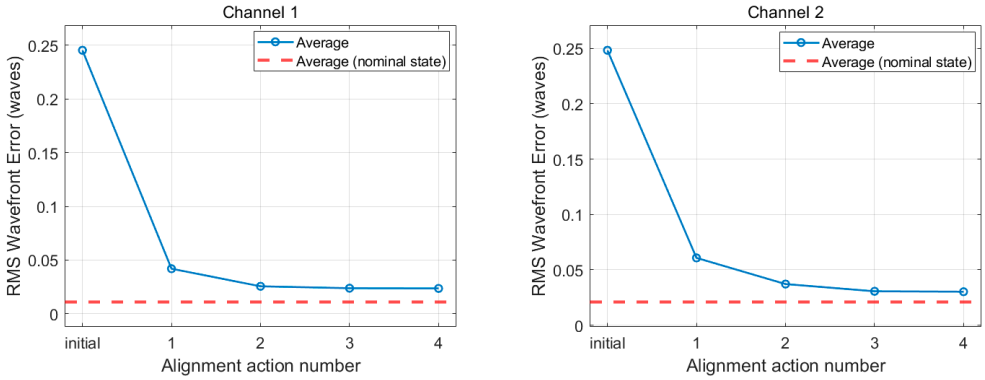

(**a**) (**b**)

Figure 5. Results of WFE of the two channels after each alignment. (**a**) Channel 1, (**b**) Channel 2.

As seen in Figure 5, the RMS WFE decreases significantly after the first aberration compensation. The RMS WFE values reach a stable state after the second aberration compensation, approaching the design level.

A Monte Carlo simulation method was employed to evaluate the robustness and performance of the compensation algorithm by introducing random perturbations into the misalignment parameters. The RMS WFE is selected as the evaluation criterion. For each trial in the Monte Carlo analysis, the average RMS WFE over the full field is calculated after compensation to assess the effectiveness of the simulation alignment process. The random misalignment ranges used are listed in Table 5.

Table 5. Random misalignments of the SM and TM.

	XDE (mm)	YDE (mm)	ADE (°)	BDE (°)
SM	[−0.1, 0.1]	[−0.1, 0.1]	[−0.01, 0.01]	[−0.01, 0.01]
TM_1	[−0.1, 0.1]	[−0.1, 0.1]	[−0.01, 0.01]	[−0.01, 0.01]
TM_2	[−0.1, 0.1]	[−0.1, 0.1]	[−0.01, 0.01]	[−0.01, 0.01]

Within the given misalignment ranges, 200 sets of misalignment states were randomly generated following a uniform distribution. Additionally, in a real alignment environment, various factors affect the measurement accuracy of the Zernike coefficients. To simulate

this situation, the noise model shown in Equation (24) was used to introduce wavefront measurement errors during the alignment process.

$$e = N(\mu = 0, \sigma = 0.03) \tag{24}$$

where $N(\mu, \sigma)$ represents a normal distribution with a mean μ and a standard deviation of σ, simulating random noise caused by uncertain factors such as temperature gradients and vibration.

Figure 6 shows the average full-field RMS WFE results. The red data points represent the average RMS WFE for the misaligned system, while the blue points represent the average RMS WFE after compensation. As observed in Figure 6, the average RMS WFE after the second compensation converges to approximately 0.022λ for Channel 1 and 0.034λ for Channel 2 under different misalignment conditions. The simulation results show that the proposed analytic method for the simultaneous compensation of dual-channel misalignment aberrations is feasible and significantly improves the optical performance of the system.

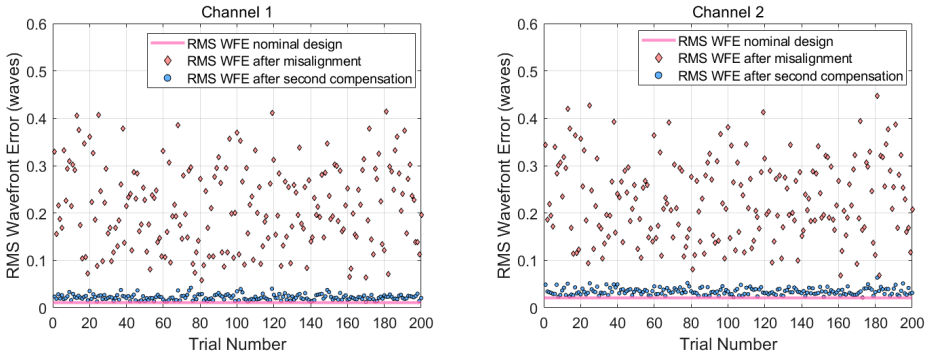

(**a**) (**b**)

Figure 6. RMS WFE of the two channels based on NAT. (**a**) Channel 1, (**b**) Channel 2.

4.2. Comparison Experiment

In this section, we compare the proposed method with the SMM. The SMM is commonly used in engineering. It is a matrix composed of the partial derivatives of the Zernike coefficients with respect to misalignment quantities, expressed as

$$\begin{bmatrix} \Delta C_1 \\ \vdots \\ \Delta C_i \\ \vdots \end{bmatrix} = \begin{bmatrix} C_1(N + \Delta M) \\ \vdots \\ C_i(N + \Delta M) \\ \vdots \end{bmatrix} - \begin{bmatrix} C_1(N) \\ \vdots \\ C_i(N) \\ \vdots \end{bmatrix} = \begin{bmatrix} \frac{\partial C_1(N)}{\partial x_1} & \frac{\partial C_1(N)}{\partial x_2} & \cdots & \frac{\partial C_c(N)}{\partial x_n} \\ \vdots & \vdots & \vdots & \vdots \\ \frac{\partial C_i(N)}{\partial x_1} & \frac{\partial C_i(N)}{\partial x_2} & \cdots & \frac{\partial C_i(N)}{\partial x_n} \\ \vdots & \vdots & \vdots & \vdots \end{bmatrix} \begin{bmatrix} \Delta m_1 \\ \vdots \\ \Delta m_i \\ \vdots \end{bmatrix} \tag{25}$$

To determine the common compensation position for the dual-channel system, we cannot solve for each channel independently, as the SM acts on both channels simultaneously. Instead, we constructed a globally coupled sensitivity matrix. When the two channels are compensated simultaneously, the optimal position of the SM is estimated based on the least squares algorithm. As shown in Figure 7, the average RMS WFE converges to approximately 0.031λ for Channel 1 and 0.036λ for Channel 2. Both channels exhibit lower optical performance compared to that of NAT.

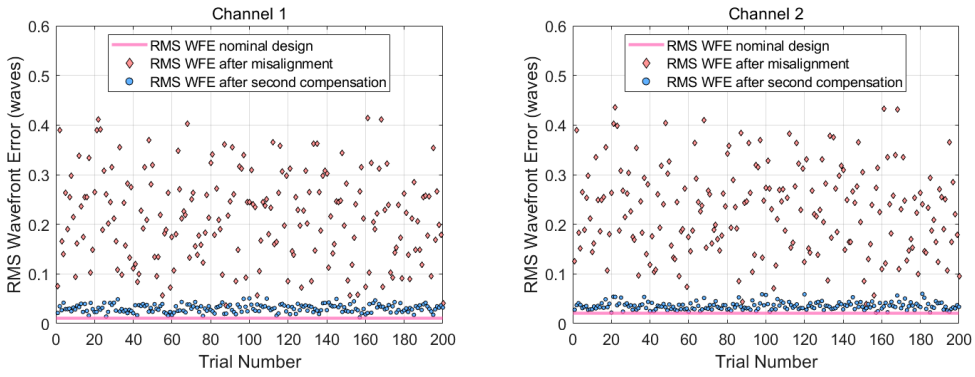

(**a**) (**b**)

Figure 7. RMS WFE of the two channels based on SMM. (**a**) Channel 1, (**b**) Channel 2.

Furthermore, to evaluate the compensation accuracy of misalignment aberrations, the Root Mean Square Deviation (RMSD) was introduced to quantify the magnitude of the residual aberrations. The RMSD can be expressed as

$$RMSD = \sqrt{\frac{1}{200}\sum_{i=1}^{200}\left(RMS_{i,alignmemt} - RMS_{i,nominal}\right)^2} \tag{26}$$

where $RMS_{i,alignmemt}$ represents the residual RMS WFE, and $RMS_{i,nominal}$ represents the nominal average RMS WFE.

The average compensation accuracy of the two channels is defined as

$$RMSD_{mean} = \sqrt{\frac{1}{400}\left[\sum_{i=1}^{200}\left(RMS_{i,c1,alignmemt} - RMS_{i,c1,nominal}\right)^2 + \sum_{i=1}^{200}\left(RMS_{i,c2,alignmemt} - RMS_{i,c2,nominal}\right)^2\right]} \tag{27}$$

The calculation results are shown in Table 6.

Table 6. RMSD values based on NAT and SMM.

	Channel 1	Channel 2	Mean Value
NAT	0.0125λ	0.0153λ	0.0140λ
SMM	0.0209λ	0.0163λ	0.0187λ

It can be seen from Table 6 that the RMSD values achieved by the proposed method in this paper are superior across both channels, and the average compensation accuracy of the two channels is improved by 25.5% compared to that of the SMM.

4.3. Simulation Results Considering Surface Figure Errors

In practical engineering applications, in addition to positional misalignments, surface figure errors also contribute to the aberration field. The interferometric measurement results of the surface figure errors are presented in Figure 8.

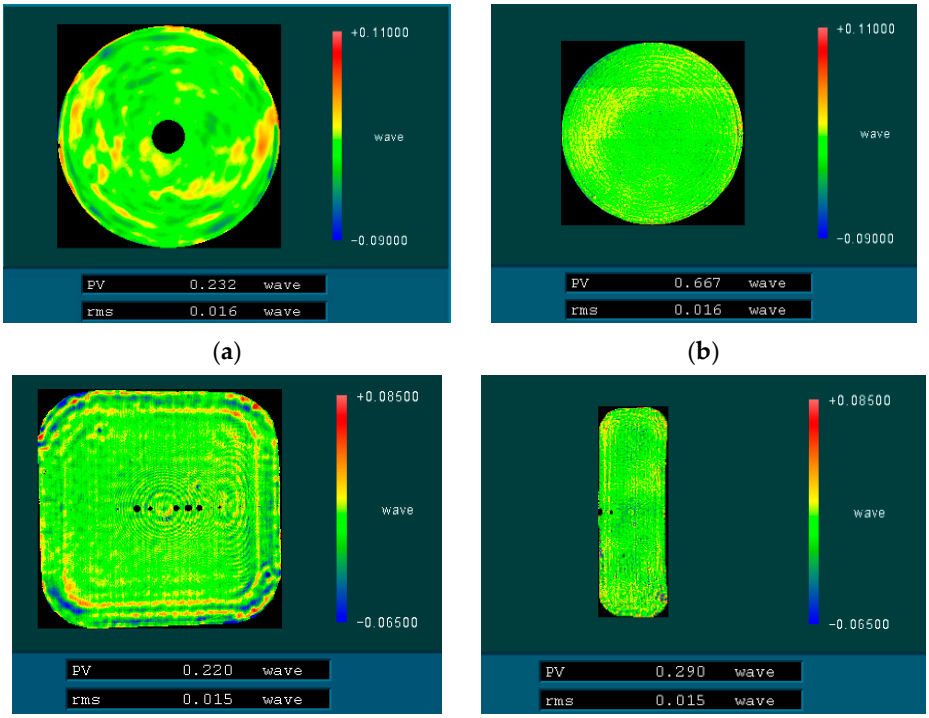

Figure 8. Interferometric measurement results. (**a**) Surface figure error of PM, (**b**) surface figure error of SM, (**c**) surface figure error of TM_1, (**d**) surface figure error of TM_2.

Incorporating surface figure errors, the RMS WFE of the system is shown in Figure 9.

Within the given misalignment ranges specified in Table 5, a Monte Carlo simulation analysis was conducted considering random noise and surface figure errors. As shown in Figure 10, using the NAT-based method, the average RMS WFE converges to approximately 0.047λ for Channel 1 and 0.062λ for Channel 2 under different misalignment conditions.

As shown in Figure 11, the average RMS WFE using SMM converges to approximately 0.054λ for Channel 1 and 0.062λ for Channel 2 under different misalignment conditions.

The calculation results of RMSDs are shown in Table 7.

Table 7. RMSD values based on NAT and SMM considering surface figure errors.

	Channel 1	Channel 2	Mean Value
NAT	0.0055λ	0.0085λ	0.0072λ
SMM	0.0119λ	0.0106λ	0.0113λ

It can be seen from Table 7 that the method based on NAT achieves higher accuracy in compensating for the aberrations of the two channels, and the average compensation accuracy of the two channels is improved by 36.5% compared to that of the SMM. Furthermore, the residuals after compensation by both algorithms are further reduced relative to the initial state with surface figure errors. This is attributed to the fact that the SM also partially compensates for low-order aberrations caused by figure errors.

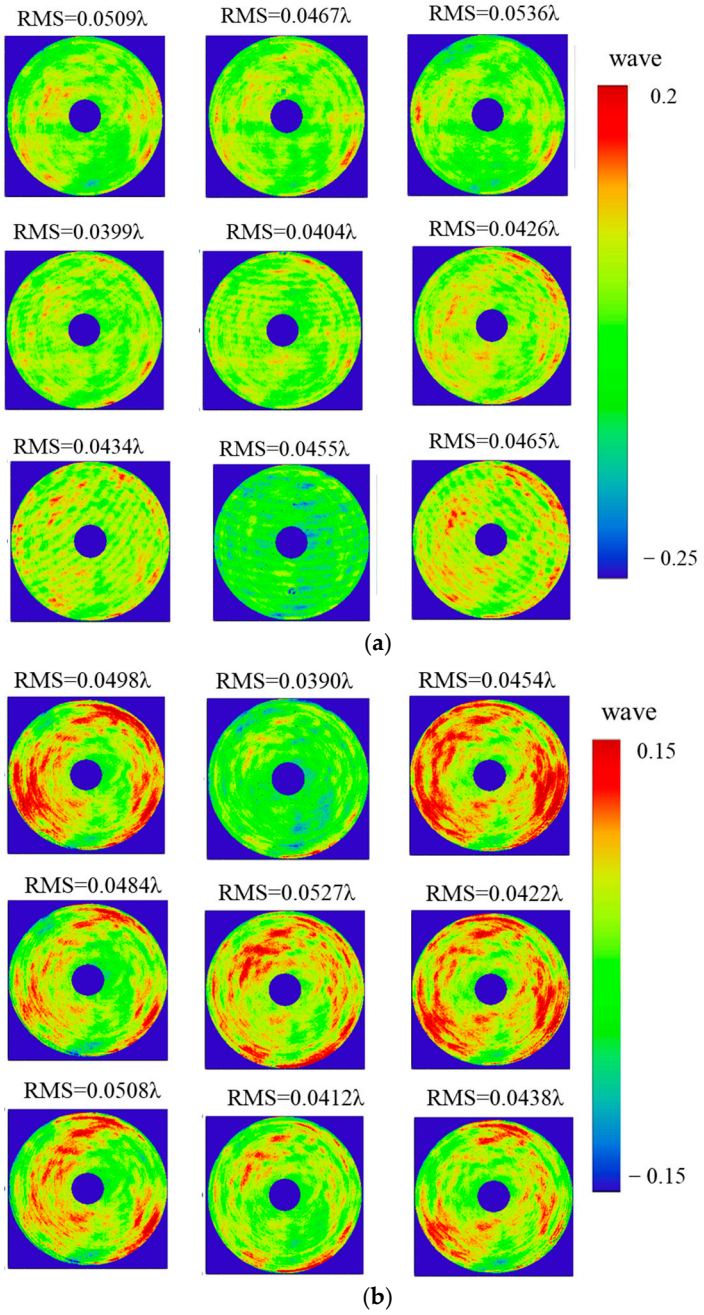

Figure 9. RMS WFE of the system. (**a**) Channel 1, (**b**) Channel 2.

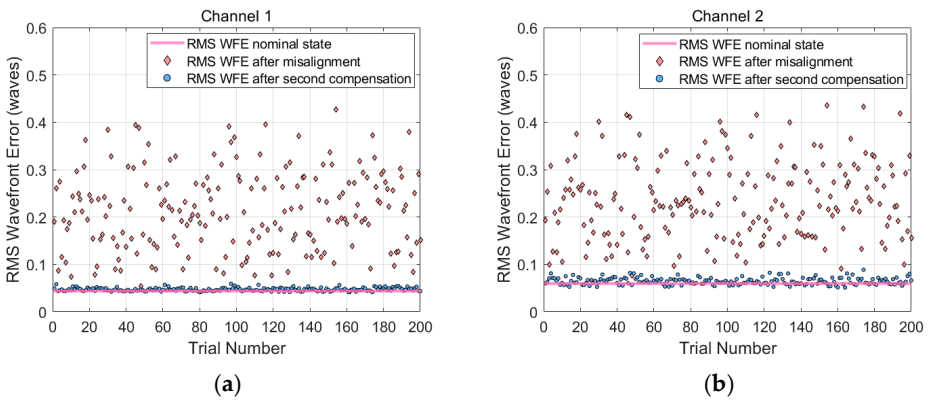

(**a**) (**b**)

Figure 10. RMS WFE of the two channels based on NAT considering surface figure errors. (**a**) Channel 1, (**b**) Channel 2.

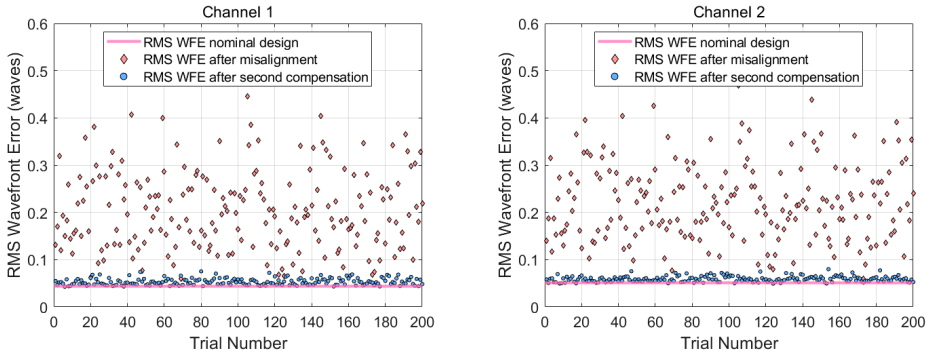

(**a**) (**b**)

Figure 11. RMS WFE of the two channels based on SMM considering surface figure errors. (**a**) Channel 1, (**b**) Channel 2.

4.4. Discussion

The superiority of the proposed NAT-based method over the traditional SMM in improving the image quality of the dual-channel system has been demonstrated in the simulation results. This performance gap can be attributed to two fundamental factors. First, the NAT-based method utilizes the inherent physical distribution characteristics of aberration fields to achieve low sensitivity to small system perturbations and enhanced robustness, facilitating effective aberration correction for complex optical systems. Second, in terms of solution stability relative to existing studies [6–8], SMM relies on numerical calculations based on the least squares method to determine the simultaneous compensation position for the sampling points within the FOV. Consequently, the setting of FOV weighting factors affects the optimization results, making it difficult to empirically determine the most suitable factors for achieving a global optimal solution. In contrast, our work extends the application of NAT, which was previously limited to single channel alignment [13–17], to the simultaneous balancing of dual-channel systems. NAT demonstrates that the positions of the aberration nodes are deterministic. It ensures high imaging quality across the entire system through the geometric balancing of the nodes relative to the two channels.

Furthermore, the adjustment of the secondary mirror primarily modifies the low-order aberration fields. Consequently, the proposed method covers the compensation for misalignments and the low-order components of figure errors. However, high-order aberrations induced by complex figure errors cannot be completely corrected by these secondary mirror adjustments and will remain as residual errors in the system.

5. Conclusions

In this paper, an analytic compensation strategy using a shared SM for perturbed common-aperture dual-channel telescopes is established based on the improved NAT. Unlike traditional numerical approaches, this method utilizes the geometric characteristics of aberration field nodes to harmonize the conflicting compensation requirements of the two channels. On this basis, the theoretical conditions for the consistency of optimal compensation between the dual channels are derived. To validate the robustness of the method, Monte Carlo simulations are conducted, considering both random noise and surface figure errors. The results show that the RMS WFE of both channels is successfully reduced to less than $\lambda/16$. Furthermore, comparative analysis with the SMM shows that the average compensation accuracy of the two channels is improved by 36.5%, demonstrating that the proposed method outperforms the SMM in terms of accuracy and decoupling capability. This work provides a deterministic theoretical strategy for the active alignment

of complex space optical systems, offering significant potential for future applications in high-precision space telescopes.

Author Contributions: Conceptualization, M.X. and D.X.; methodology, M.X.; software, M.X. and Q.W.; validation, M.X. and Q.W.; formal analysis, M.X. and Y.Y.; investigation, M.X.; resources, D.X. and X.Z.; data curation, M.X.; writing—original draft preparation, M.X.; writing—review and editing, Y.Y., W.D., D.X. and X.Z.; visualization, M.X. and Q.W.; supervision, D.X. and X.Z.; project administration, X.Z.; funding acquisition, W.D. All authors have read and agreed to the published version of the manuscript.

Funding: This research was funded by the National Natural Science Foundation of China (62375260) and CAS Youth Interdisciplinary Team (2023-135).

Institutional Review Board Statement: Not applicable.

Informed Consent Statement: Not applicable.

Data Availability Statement: Data underlying the results presented in this paper are not publicly available at this time but may be obtained from the authors upon reasonable request.

Conflicts of Interest: The authors declare no conflicts of interest.

References

1. Wen, M.; Han, C.; Ma, H. Active Compensation for Optimal RMS Wavefront Error in Perturbed Off-Axis Optical Telescopes Using Nodal Aberration Theory. *Appl. Opt.* **2021**, *60*, 1790. [CrossRef]
2. Zhang, Z.; Dong, B. Field-Balancing Alignment of the Secondary Mirror of Space Telescope Using a Self-Calibrated Model. *Opt. Commun.* **2024**, *563*, 130619. [CrossRef]
3. Li, B.; Zhang, X.; Gu, Y.; Zhao, S.; Chang, J. Active Compensation for Perturbed Coaxial Reflecting Space Telescope Using Defocus Point Spread Function and Convolutional Neural Network. *Opt. Commun.* **2023**, *537*, 129451. [CrossRef]
4. Huang, C.; Li, J.; Cai, Z.; Yu, J.; Xie, Y.; Mao, X. Post Optical Freeform Compensation Technique for Machining Errors of Large-Aperture Primary Mirror. *Photonics* **2023**, *10*, 768. [CrossRef]
5. Zhang, X.; Zhang, D.; Xu, S.; Ma, H. Active Optical Alignment of Off-Axis Telescopes Based on Nodal Aberration Theory. *Opt. Express* **2016**, *24*, 26392. [CrossRef]
6. Oh, E.; Ahn, K.-B.; Kim, S.-W. Experimental Sensitivity Table Method for Precision Alignment of Amon-Ra Instrument. *J. Astron. Space Sci.* **2014**, *31*, 241–246. [CrossRef]
7. Zhu, B.; Bai, X.; Wang, S.; Zhang, C.; Jiang, F.; Gao, Y.; Xu, S.; Ju, G. Single-Field-of-View Misalignment Solution Method Based on Map Sensitivity Matrix. *Opt. Express* **2025**, *33*, 16562. [CrossRef] [PubMed]
8. Hou, H.; Ding, H.; Dong, K.; Cao, G.; Wang, B. A Method for Mounting Space Telescope Optical Systems Based on the Sensitivity Matrix of Intrinsic Coefficients. *Sensors* **2025**, *25*, 1121. [CrossRef]
9. Thompson, K.P.; Schmid, T.; Cakmakci, O.; Rolland, J.P. Real-Ray-Based Method for Locating Individual Surface Aberration Field Centers in Imaging Optical Systems without Rotational Symmetry. *J. Opt. Soc. Am. A* **2009**, *26*, 1503. [CrossRef]
10. Schmid, T.; Thompson, K.P.; Rolland, J.P. Misalignment-Induced Nodal Aberration Fields in Two-Mirror Astronomical Telescopes. *Appl. Opt.* **2010**, *49*, D131. [CrossRef]
11. Yeşiltepe, M.; Bauer, A.; Karcı, Ö.; Rolland, J.P. Sigma Vector Calculations in Nodal Aberration Theory and Experimental Validation Using a Cassegrain Telescope. *Opt. Express* **2023**, *31*, 42373. [CrossRef]
12. Moore, L.B.; Hvisc, A.M.; Sasian, J. Aberration Fields of a Combination of Plane Symmetric Systems. *Opt. Express* **2008**, *16*, 15655. [CrossRef]
13. Wang, J.; He, X.; Luo, J.; Zhang, X.; Xu, T. Alignment Algorithm of Nonsymmetric Off-Axis Reflective Astronomical Telescopes Based on the Modified Third-Order Nodal Aberration Theory. *Opt. Express* **2022**, *30*, 13159. [CrossRef]
14. Sebag, J.; Gressler, W.; Schmid, T.; Rolland, J.P.; Thompson, K.P. LSST Telescope Alignment Plan Based on Nodal Aberration Theory. *Publ. Astron. Soc. Pac.* **2012**, *124*, 380–390. [CrossRef]
15. Zhang, X.; Xu, S.; Ma, H.; Liu, N. Optical Compensation for the Perturbed Three Mirror Anastigmatic Telescope Based on Nodal Aberration Theory. *Opt. Express* **2017**, *25*, 12867. [CrossRef]
16. Bai, X.; Xu, B.; Ju, G.; Ma, H.; Zhang, C.; Wang, S.; Xu, S. Aberration Compensation Strategy for the Radius of Curvature Error of the Primary Mirror in Off-Axis Three-Mirror Anastigmatic Telescopes. *Appl. Opt.* **2021**, *60*, 6199. [CrossRef] [PubMed]
17. Bai, X.; Gu, X.; Xu, B.; Jiang, F.; Lu, Z.; Xu, S.; Ju, G. Active Alignment of Large-Aperture Space Telescopes for Optimal Ellipticity Performance. *Sensors* **2023**, *23*, 4705. [CrossRef]

18. Thompson, K.P.; Schmid, T.; Rolland, J.P. The Misalignment Induced Aberrations of TMA Telescopes. *Opt. Express* **2008**, *16*, 20345. [CrossRef]
19. Thompson, K. Description of the Third-Order Optical Aberrations of near-Circular Pupil Optical Systems without Symmetry. *J. Opt. Soc. Am. A* **2005**, *22*, 1389. [CrossRef] [PubMed]
20. Thompson, K.P. Multinodal Fifth-Order Optical Aberrations of Optical Systems without Rotational Symmetry: The Comatic Aberrations. *J. Opt. Soc. Am. A* **2010**, *27*, 1490. [CrossRef] [PubMed]
21. Thompson, K.P. Multinodal Fifth-Order Optical Aberrations of Optical Systems without Rotational Symmetry: The Astigmatic Aberrations. *J. Opt. Soc. Am. A* **2011**, *28*, 821. [CrossRef] [PubMed]
22. Gray, R.W.; Rolland, J.P. Wavefront Aberration Function in Terms of R V Shack's Vector Product and Zernike Polynomial Vectors. *J. Opt. Soc. Am. A* **2015**, *32*, 1836. [CrossRef] [PubMed]
23. Gu, Z.; Yan, C.; Wang, Y. Alignment of a Three-Mirror Anastigmatic Telescope Using Nodal Aberration Theory. *Opt. Express* **2015**, *23*, 25182. [CrossRef] [PubMed]